# Laser-patterned thin-film electrodes

## Imaging ion accumulation and trapped nanoparticles

Dogru Yuksel, Itir Bakis; Zhang, Zhu; Vreugdenhil, Marnix; Mosk, Allard P.; van Oosten, Dries; Faez, Sanli

**DOI**
10.1063/5.0251717

**Publication date**
2025

**Document Version**
Final published version

**Published in**
APL Photonics

APL Photonics

RESEARCH ARTICLE | AUGUST 06 2025

# Laser-patterned thin-film electrodes: Imaging ion accumulation and trapped nanoparticles

Itir Bakis Dogru Yuksel ; Zhu Zhang ; Marnix Vreugdenhil ; Allard P. Mosk ; Dries van Oosten ; Sanli Faez



*APL Photonics* 10, 086103 (2025)
https://doi.org/10.1063/5.0251717

# Laser-patterned thin-film electrodes: Imaging ion accumulation and trapped nanoparticles

Cite as: APL Photon. 10, 086103 (2025); doi: 10.1063/5.0251717
Submitted: 4 December 2024 • Accepted: 11 July 2025 •
Published Online: 6 August 2025



Itir Bakis Dogru Yuksel,[1,2,a)] Zhu Zhang,[1,3] Marnix Vreugdenhil,[1] Allard P. Mosk,[1] Dries van Oosten,[1] and Sanli Faez[1]

## AFFILIATIONS

[1] Debye Institute for Nanomaterials Science, Utrecht University, Utrecht, The Netherlands
[2] Department of Microelectronics, Delft University of Technology, Delft, The Netherlands
[3] Sorbonne Université, Institut de la Vision, Paris, France

[a)] **Author to whom correspondence should be addressed:** i.b.dogru@tudelft.nl

## ABSTRACT

This study introduces a straightforward electrode design featuring sharp edges with a curvature of a few hundred nanometers in radius, with which both ion accumulation and nanoparticle deposition can be observed under an alternating electrical potential. The electrodes, termed "shark-teeth electrodes," are fabricated using a laser ablation technique optimized for facile nanostructure creation. This method involves successive, overlapping ablated disks in a thin-film of gold, producing sharp tips that generate strong electric fields. When electrically polarized in an electrolyte solution, these sharp tips form a screening layer, facilitating the observation of ion and nanoparticle behavior. A total-internal reflection microscope is employed to monitor ion accumulation on these electrodes, demonstrating their capability in iontronic microscopy. In addition, the same electrodes are used to track nanoparticle trapping under high-frequency alternating potentials. This dual functionality allows for the investigation of electrochemical and physical interactions between ions and colloidal nanoparticles, which provide valuable insights into soft matter systems, including biological systems such as cells, where similar interactions play a crucial role.





## I. INTRODUCTION

The manipulation and real-time observation of solvated ions and colloidal nanoparticles in liquids have applications in multiple disciplines, from environmental protection to technological innovation and life sciences. Such control facilitates pollutant removal, supporting cleaner ecosystems,[1] and enables the tuning of key material properties—such as electrical conductivity,[2] thermal behavior,[3] and optical characteristics[4]—thereby driving innovation in advanced materials. In biophysics, controlling ion and particle movement is pivotal.[5,6] It drives research on molecular biology,[7] yielding insights into cell behavior[8] and innovation such as lab-on-a-chip devices[9] for advancing biomedical investigations.[10–12]

A common method for manipulating colloidal species involves using an electric field, where the electrode design is critical for controlling the dynamics of ions[13,14] and particles.[15,16] Recent studies have highlighted the importance of electrode design for innovative biomedical applications. Sy *et al.* proposed an electrokinetic chip utilizing a ring-shaped interdigitated electrode for rapidly collecting particles for fast bacterial counting.[17] Zhou *et al.* introduced a template electrokinetic assembly to showcase microparticle assembly at specific positions.[18] Ji *et al.* created a 3D model to analyze particle positions for cell manipulation.[19] In addition, Varmazyari *et al.* developed a microfluidic system for cancer cell separation.[20] Furthermore, an electrochemical molecule trap within a nanopipette enables ultrasensitive detection of enzyme activity in single cells via electro-osmotic flow.[21] Non-electrical techniques, such as optical trapping[22] and acoustic trapping,[23] also allow for precise control of particle positioning. However, these approaches often involve complex instrumentation, limited scalability, or sensitivity to particle properties. Moreover, they do not provide the ability to observe ion accumulation dynamics at the liquid–solid interface, a key feature for studying electrokinetic behavior. The ability to release particles on demand maintains uninterrupted analyses, preventing system

clogging.[24] This approach facilitates continuous monitoring of cellular processes, which is essential for understanding particle dynamics in biological contexts.

Optical microscopy techniques enable detailed observation of ion redistribution at the liquid–solid interface in response to an applied electric field. These methods reveal potentiodynamic optical contrast—variations in optical signals corresponding to changes in local ionic environments—thereby complementing the spatial and functional understanding offered by electrode design. Ion currents are inferred from total-internal-reflection (TIR) microscopy[25,26] and interferometric reflection microscopy[27] across various electrode configurations, where image analysis reveals ion accumulation. Previous approaches, such as that by Merryweather *et al.*, while elegantly capturing ion dynamics in-operando using optical contrast, investigated immobilized microparticles, thereby requiring static conditions and making it challenging to obtain data under dynamic conditions with a single configuration.[28] Similarly, most optical studies focus on either ion dynamics or on fixed components.[29] There is no platform that enables the simultaneous, dynamic trapping of mobile particles alongside local ionic mapping in a single setup.

In this study, we introduce a new electrode design that facilitates the simultaneous monitoring of both the movements of ions and nanoparticles. Our planar electrodes are fabricated via an optimized laser ablation method, producing symmetrical, sharp-patterned gold electrodes, referred to as "shark-teeth electrodes," named because of the sharp tips formed between successively ablated circles in a thin gold film, which are capable of generating strong electric fields. This laser ablation technique is a facile method for creating flat nanoelectrodes, with high throughput, rapid turnaround, and no need for cleanroom facilities.

We employed these "shark-teeth electrodes" to analyze the electrophoretic frequency-dependent behavior of solvated species, ranging from ions to nanoparticles. By imaging the movement of ions and particles at various frequencies using TIR scattering and fluorescence microscopy, we provide detailed insights into the mechanisms governing their behavior. Our findings demonstrate that under an alternating current (AC) potential application at low frequencies (up to tens of Hz), both ions and nanoparticles oscillate due to electric double layer (EDL) modulation at the electrode nanoedges.[25] However, at higher frequencies, the EDL does not have sufficient time to establish,[30] and the signal from ions diminishes. At these frequencies, the stronger electric field gradient formed at the sharp tips dominates nanoparticle drift motion and attracts them to these edges due to the dielectrophoresis (DEP)[31] effect.

Simultaneously monitoring ions and nanoparticles using shark-teeth electrodes holds promising implications for biological applications. These electrodes could be integrated into organs-on-a-chip devices,[32] enabling real-time analysis of intricate biological processes. For example, their ability to track drug delivery[33,34] at specific tissue sites could enhance precision in nanoparticle-based cancer treatments while minimizing side effects. In addition, by precisely monitoring ion concentrations, these electrodes simulate physiological environments, making them valuable tools for studying tissue behavior and disease progression.[35,36] Incorporating ion and particle tracking alongside transepithelial or transendothelial electrical resistance (TEER) measurements[37] enhances the ability to monitor tissue integrity, permeability, and overall function, providing comprehensive data about barrier function and offering significant advantages in clinical diagnostics.[38]

## II. RESULTS AND DISCUSSION

### A. Shark-teeth electrode fabrication

The planar thin-film electrodes were fabricated on a thin cover slide, featuring an H-shaped metallic coating composed of a targeted 1 nm chromium adhesion layer and a 10 nm gold conductive layer for improved transparency [Fig. 1(a)]. The metallic surface was then separated into two electrodes (Fig. S1) using laser ablation, with successive femtosecond laser pulses (a central wavelength of 1034 nm and a pulse duration of 170 ps) focused onto the gold surface while it was moved horizontally through the laser focus [Fig. 1(b)]; the setup for this process is detailed in Fig. S2. This process resulted in the creation of features with sharp corners, resembling the structure of shark-teeth [Figs. 1(c) and 1(d)]; hence, we referred to them by that name. This design enhances electric field generation, particularly at the sharp tips. The characterization of the developed electrodes, customized for investigating ion accumulation and trapping nanoparticles under potential modulation, involves the use of TIR microscopy,[26,39,40] where the electric potential is generated via a wavefunction generator [Fig. 1(e)]. Using TIR configuration instead of bright-field reflection helps by preventing the detection saturation in the camera and allows for optimal use of the dynamic range of the camera for detecting the interference signal of light scattered from the ions around the nanoparticles and the (much) larger scattering from the nanoparticle, which here acts as a reference arm of an interferometer. We use a gasket to introduce the electrolyte and particle solutions between the electrodes and use a disk-shaped glass slide to cover the gasket and suppress solvent evaporation [Fig. 1(f)]. Figure 1(g) highlights the details of the electrodes through Scanning Electron Microscopy (SEM) images. The ultrafast nature of laser pulses is crucial for inducing the observed folding at the edges of the gold layer, as depicted in Fig. 1(g). Unlike longer laser pulses, femtosecond pulses do not lead to melting. Rather, the rapid energy deposition initiates an inertial heating process that leads to elasto-plastic deformation of the gold film, causing the material to detach and form flaps.[41] The periodicity of the sharp edges of symmetrical electrodes, shown in Fig. 1(h), is calculated based on the distance between the centers of the elliptical laser ablation regions, averaging 4.948 $\mu$m with a standard deviation of 0.487 $\mu$m. The longest diameter of each elliptical ablation region is 7.188 ± 0.435 $\mu$m. Both measurements are based on a statistical analysis of 30 pattern repetitions, as shown in Fig. S3, where the bar graphs illustrate the distributions and variances. Variations in laser positioning likely cause the horizontal stretching observed in the pattern. In addition, the visualization of the sample using TIR microscopy is presented in Fig. 1(i), where the electrolyte solution is on top.

### B. Imaging ion concentration oscillations induced by the applied potential

In this section, we investigate the ion current between the gap of the shark-teeth electrodes in an aqueous solution with 0.1 M potassium chloride (KCl) electrolyte when an AC potential is applied in the square waveform at 5 Hz and 1 V peak-to-peak. We intentionally applied low frequency to allow for the formation of the EDL and

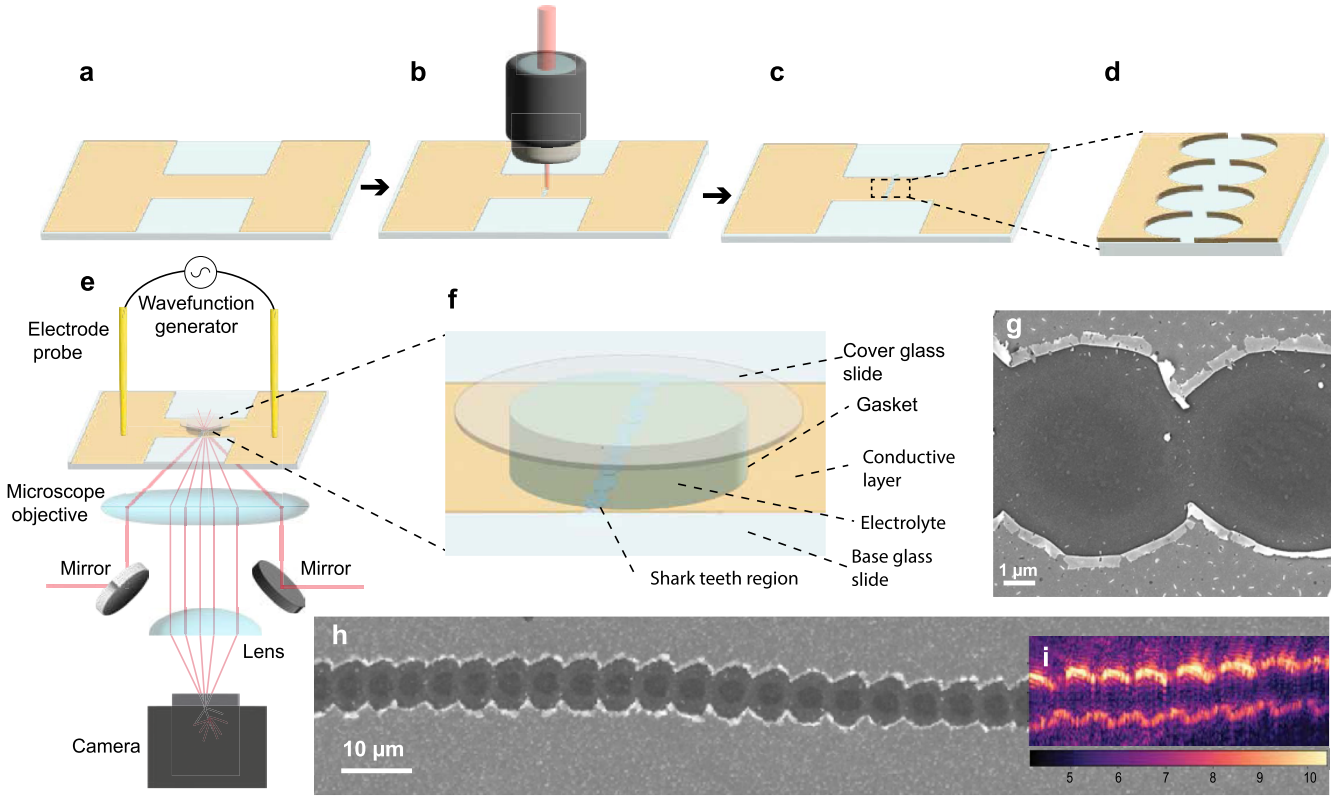


**FIG. 1.** Shark-teeth electrode fabrication and ion flow analysis setup (schematics not drawn to scale). (a) H-shaped conductive layer coated on a glass slide. (b) Laser ablation etching of the mid-region. (c) Resulting laser-ablated planar electrodes, and (d) with a zoomed version for detail. (e) Schematic of the ion flow analysis setup: ion flow is induced by a wavefunction generator through electrode probes on both of the shark-teeth electrodes and imaged by a TIR microscope. (f) Schematic of the shark-teeth electrodes depicting the electrolyte insertion between them within a gasket, covered by a glass slide. SEM images (g) showcasing the shark-teeth electrodes with sharp edges and (h) highlighting the periodicity of the sharp edges on both electrodes. (i) TIR microscopy image showing the structure of shark-teeth electrodes under static conditions, with no electric field applied.

to observe changes in ion concentration. The peak-to-peak voltage was limited to 1 V to remain within the electrochemical stability window of water (1.23 V[42]). This precaution minimizes the risk of Faradaic reactions and water splitting at the electrode tips, thereby ensuring that the observed signals result solely from ion accumulation under AC excitation. We recorded a video by TIR microscopy during the potential application to the shark-teeth electrode with KCl electrolyte solution on and between the electrodes. Then, the ion accumulation information was extracted from the series of frames (multimedia available online; see Video 1 of the supplementary material for the periodic twinkling from the electrodes).

Two square regions, each corresponding to 360 × 360 $nm^2$ and marked in green and violet, respectively [Fig. 2(a)], were chosen for further examination—each positioned on opposite electrodes across the shark-teeth region. To provide additional structural context, we have overlaid a transparent SEM image from an identically fabricated structure, where the electrodes and laser-ablated region are clearly labeled. The observed intensity changes, attributed to periodic EDL modulation synchronized with the applied potential, reflect the local ion concentration around the shark-teeth, creating an optical contrast. In other words, we observe the potentiodynamic optical contrast resulting from the accumulation of ions during the reconfiguration of the EDL[25] undergoing the potential modulation. This periodic contrast change enables us to observe dynamic scattering signal variations from anions and cations, which arise from their distinct optical polarizability and, hence, effective refractive indices.[27]

The scattering intensity observed from each electrode in Figs. 2(b) and 2(c) shows a periodic, out-of-phase relationship, both synchronized with the applied potential. This phase alignment is also evident in Figs. 2(d) and 2(e), with the corresponding potential waveform shown in Fig. 2(f). The dynamic behavior is more clearly illustrated in Video 1 of the supplementary material (multimedia available online), from which these figures were extracted. The consistent minimum and maximum values that fluctuate periodically over time in Figs. 2(d) and 2(e), without any significant deviations, indicate that the observed changes are not a result of electrode deformation. If deformation were present, we would expect to see notable shifts in these values, further underscoring the reliability of our electrode. We would like to clarify that

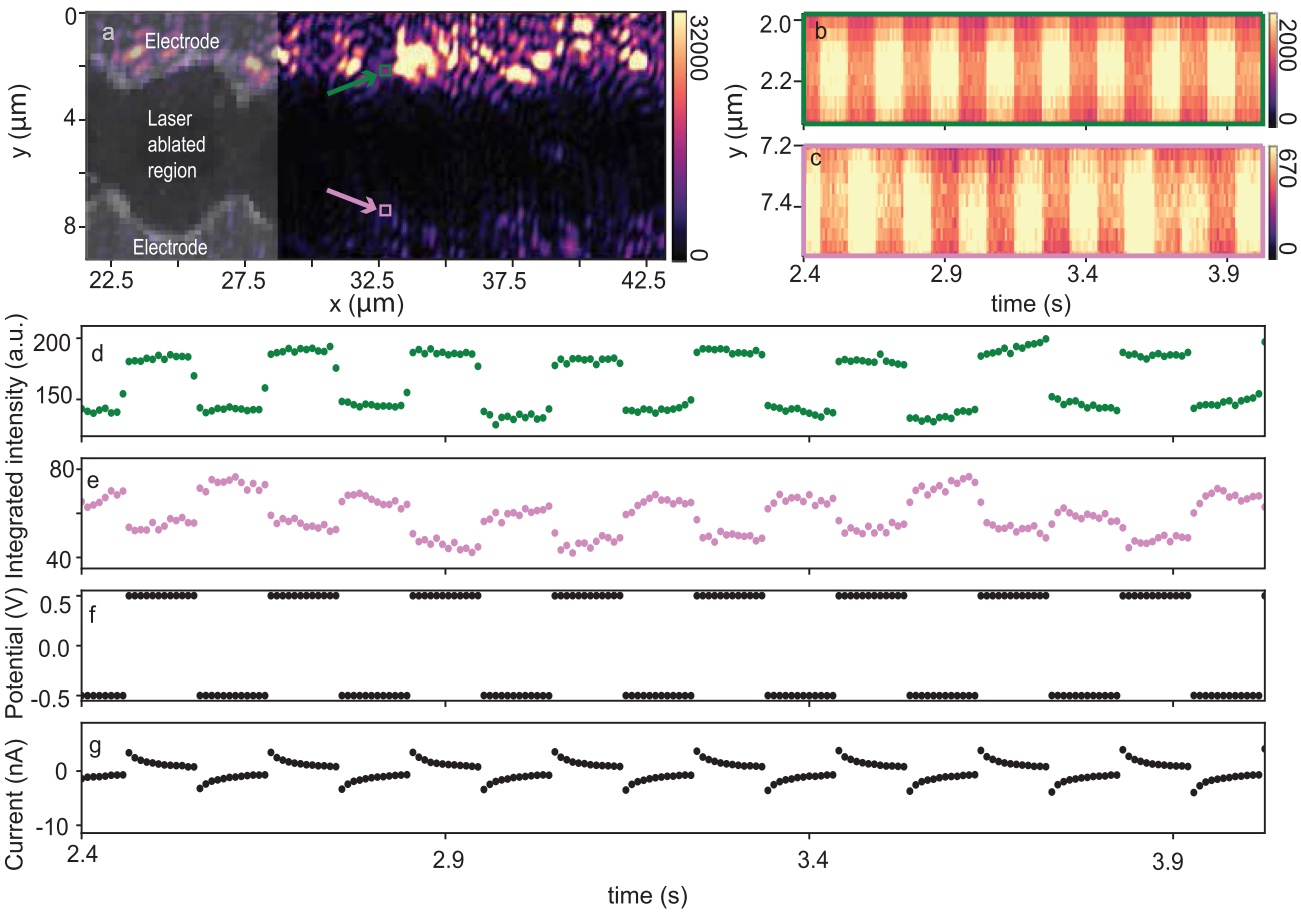


**FIG. 2.** Real-time analysis of ion flow with scattering via shark-teeth electrode. (a) The shark-teeth electrode image by scattering under the influence of a 5 Hz, 1 V peak-to-peak square waveform. Two distinct regions marked with green and violet squares and arrows pointing in opposite directions of the shark-teeth are selected for further examination. To assist structural interpretation, a partially overlaid transparent SEM image from an identically fabricated structure is added on the left side, labeling the electrodes and the laser-ablated region. (Multimedia available online) [(b) and (c)] Chemographs and [(d) and (e)] integrated intensities with respect to time extracted from the green and violet marked regions, respectively. Corresponding plots of (f) applied electric potential and (g) measured current confirm the in-operando ion concentration oscillations.

the amplitude differences between the integrated intensity peaks in Figs. 2(d) and 2(e) are primarily attributed to variations in the laser alignment and the inhomogeneous structure of the electrodes. As a result, the intensity distribution may fluctuate; however, the overall trend of periodic intensity changes remains visible. To further illustrate the origin of these amplitude differences, we have added a zoomed-out image of the electrodes (Fig. S4). This additional image shows a wider field of view of the illuminated region, highlighting how the scattering pattern varies spatially due to the structural nonuniformities of the electrodes. Figure 2(g) displays the measured current passing between the electrodes. The exponential decay observed in each cycle is indicative of the EDL capacitive charging. A very small residual current will be present at longer waiting times, corresponding to Faradaic electrochemical reactions. For the experiments described here, residual Faradaic current can be neglected, and we can assume that the electrode remains electrochemically inert throughout the measurement. In the supplementary material, Fig. S5 presents both Bode plots and cyclic voltammetry results, which provide detailed insights into the electrochemical properties of the system. We also conducted a control experiment comparing a 0.1M KCl solution with ultrapure water, applying the same electric field and maintaining all other experimental parameters constant (see Fig. S6). The KCl solution produced pronounced, periodic optical signals, whereas the water sample exhibited only weak variations. This contrast underscores the critical role of ion concentration in generating the observed optical responses. More regions are selected from both electrodes to show that this integrated intensity change behavior is consistent in the shark-teeth electrodes, where ion current is out-of-phase in each electrode within the corresponding applied electric potential (Fig. S7). When repeating the experiment with identical parameters but employing a triangular waveform potential instead of a square one, we observe that ion migration

intensity varies continuously over time. The maximum accumulation occurs at one electrode edge when the potential reaches the peak of the triangular waveform, and minimum accumulation occurs at the opposite edge when it reaches the trough (Fig. S8). In contrast, the square waveform produces alternating maximum and minimum intensities at the electrode edges in a binary manner due to abrupt polarity switching. These results highlight how the waveform shape modulates ion migration behavior in the system.

### C. Nanoparticle tracking with shark-teeth electrode

In the nanoparticle trace experiments described in this section, the electrolyte is replaced with an aqueous solution containing 200 nm fluorescent polystyrene particles. This experiment is a necessary first step toward potentiodynamic microscopy around trapped colloidal nanoparticles. Although smaller particles (down to 30 nm gold spheres in water) can be observed label-free by scattering via TIR microscopy (Video 2 of the supplementary material, multimedia available online), fluorescence microscopy is used exclusively for tracing the particles, as particle tracking with a scattering microscope is prone to a much larger error due to continuously changing background speckle. The schematic of the fluorescence microscope is shown in Fig. S9. The shark-teeth electrode is imaged via fluorescence microscopy, and the result is shown in Fig. 3(a). Here, the darker regions are the gold electrodes, and the brighter region corresponds to the gap in between. As we are not using a confocal microscope, the background fluorescence signal is much larger than each single particle. However, a single particle can be detected after subtracting the, on average, constant background. We have tracked the phoretic motion of a single nanoparticle under the application of a 1 Hz square-wave electrical potential, which is plotted in Fig. 3(b). The corresponding 3D trajectory is provided in Fig. S10 of the supplementary material. The particles cyclically approach and recede from one electrode. This particle oscillation is also shown in Video 3 of the supplementary material (multimedia available online). Some frames of that video are provided at 0.65 s [Fig. 3(c)], 1.15 s [Fig. 3(d)], 1.65 s [Fig. 3(e)], and 2.15 s [Fig. 3(f)], with previous locations fading in opacity in each subsequent frame. In these frames, shown every 0.5 s, Fig. 3(a) serves as a background and is depicted in Video 3 of the supplementary material (multimedia available online). The transparency of the thin electrode allows the particle to remain visible even when positioned beneath the conductive layers. However, after ~3 s, the particle becomes increasingly difficult to observe due to its motion in 3D space, while the imaging system captures only a 2D projection of the focal plane. This experiment shows that the nanoparticle is responding electrophoretically to the applied potential, but the force is not enough in this case to overcome the repulsive electrostatic forces between the negatively charged glass surface and the charge-stabilized colloidal particle. To reach our aim of trapping these nanoparticles at the electrode edges, we use high-frequency AC dielectrophoresis, which has previously been shown to work on other electrode geometries.[16]

### D. Trapping nanoparticles with shark-teeth electrodes

To perform iontronic microscopy on colloidal nanoparticles, we here explore the possibility of trapping them by applying an AC field at higher frequencies using the shark-teeth electrode design. Once the particle is trapped, it could be irreversible due to van der Waals forces, in which case, one can stop the AC potential and continue with the low-frequency potentiodynamic measurements. In case the van der Waals force is insufficient for capturing the particles, one can still combine the low-frequency component for EDL modulation with the high-frequency trapping. It is important to note that the Nernst–Planck–Maxwell equations governing the ion dynamics are nonlinear, and there could be mixing between low- and high-frequency responses that have to be accounted for



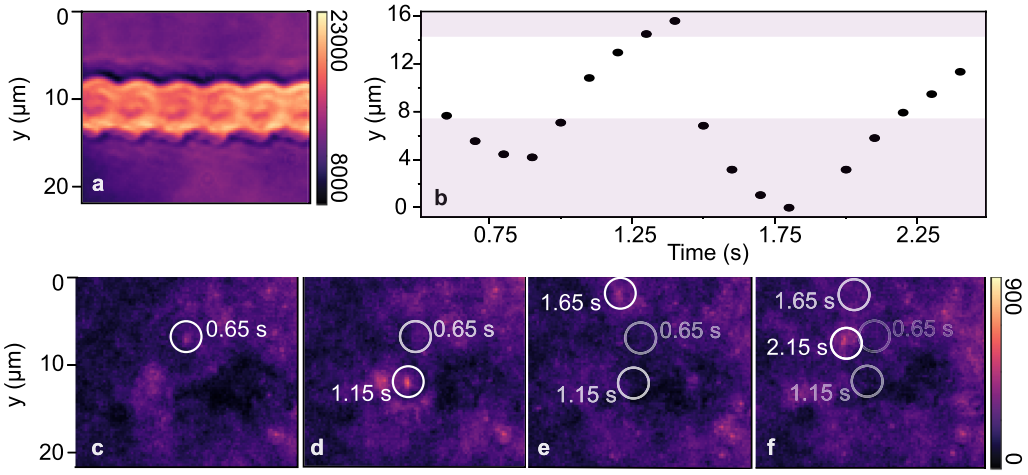


**FIG. 3.** Particle tracing with shark-teeth electrodes under a 1 Hz square wave potential application. (a) Fluorescence microscopy image showing the shark-teeth electrode and particles. (b) Projected location of the nanoparticle over time, with the purple-shaded regions indicating the electrode areas. Particles are observed even beyond the electrode due to the transparency of the material. Particles are shown at (c) 0.65 s, (d) 1.15 s, (e) 1.65 s, and (f) 2.15 s, with the same particle marked with a white ring and previous locations fading in opacity in each subsequent frame (multimedia available online). Panel (a) is extracted as a background.

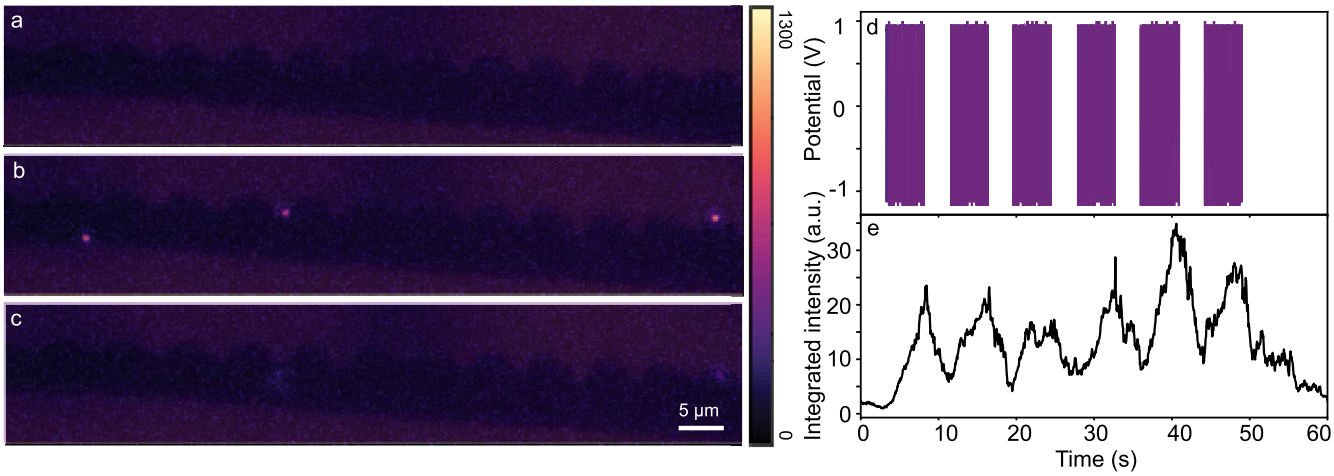


**FIG. 4.** Particle trapping within shark-teeth electrode: (a) before, (b) during, and (c) after the application of an electric field at 100 kHz. (Multimedia available online) (d) The applied potential is depicted where it is periodically terminated and initiated. (e) Integrated intensity changes during the applied potential on and off. Notably, upon application of the potential, three particles appear at the edges of the shark-teeth and vanish from the focus region when the potential is terminated.

in interpreting the results. Moreover, electro-osmosis may significantly influence the particle trapping dynamics.[43] In particular, the movement of ions in the electric field can create concentration gradients that induce osmotic flow, impacting the net movement of the particles.

We applied a 100 kHz 2 V peak-to-peak square waveform potential to the electrodes while observing the nanoparticles on the fluorescence microscope. Particles are trapped at the electrodes' sharp edges due to the electric field gradient but are released when the applied field is turned off. Studies by Hosseini *et al.*[44] and Grange *et al.*[45] demonstrated through simulations that sharp-tip electrode structures generate significant electric field gradients at the tips, supporting our design that this spatial variation enhances particle trapping near these regions. Figures 4(a)–4(c) depict the process of trapping a few nanoparticles at the sharp edges before applying the potential, during, and after turning off. In Fig. 4(c), we show the immediate release of the particles from the electrode tip once the potential is switched off, confirming the reversibility of the trapping effect. At 100 kHz, the DEP effect becomes apparent, as the gradient of the electric field exerts a force on the particles.[46] We can check the reversibility of this trapping effect by repeatedly turning the applied potential on-and-off, as shown in Fig. 4(d). Correspondingly, Fig. 4(e) illustrates the total change in the integrated fluorescence intensity around the electrode edge over time. From this measurement, most of the particles are released after each pulse, and the trapping mechanism is mostly reversible. Further details are available in Video 4 of the supplementary material (multimedia available online), where the appearance and disappearance of particles via trapping and release with the applied potential are shown. Similarly, reversible particle trapping was observed with 30 nm gold nanoparticles using TIR microscopy at higher frequencies, allowing label-free visualization of the particles via scattering (see Fig. S11 and Video 2 of the supplementary material, multimedia available online).

We mention in passing that occasionally, at an intermediate frequency of around 100 Hz, particles are absorbed strongly enough onto the electrodes and sometimes trapped irreversibly.

In these intermediate frequency regimes, rapid oscillations prevent the stable formation of the EDL, and hence, the charged colloid has a higher chance of stochastically passing through the Debye layer and getting trapped by van der Waals forces.

## III. CONCLUSION

In conclusion, this study presents a novel method for fabricating laser-drilled gold electrodes with sharp edges (shark-teeth patterns) that are suitable for trapping nanoparticles and, at the same time, allow for detecting the ion dynamics with EDL-modulation microscopy. This facile electrode fabrication can be applied to most thin-film conducting layers, including those that are not easily compatible with clean-room lithographic methods, e.g., organic conducting layers or molecular assemblies.

At low frequencies, both ions and nanoparticles oscillate primarily due to EDL modulation. TIR microscopy confirmed this behavior, showing real-time intensity changes synchronized with the applied potential. The particle can also be used as a tracer to simultaneously detect the fluid motion. As higher DEP forces, they allow for the reversible trapping of nanoparticles. We demonstrated reversible DEP-based trapping at the sharp edges of the electrodes. This transition showcases the versatility of our electrode design in controlling different electrokinetic phenomena, allowing for the manipulation of solvated species at specific positions for further analysis.

This work presents a robust and scalable method for fabricating sharp electrodes without the need for lithographical techniques. Therefore, we can envision using this fabrication technique on substrates that are not compatible with lithography. Some examples are the tip of an optical fiber or a cantilever for atomic force microscopy.

Future work will focus on extending this fabrication method to study ion dynamics and real-time ion transport processes in biological environments, such as organs-on-chips.[47]

## IV. MATERIALS AND METHODS

### A. Physical vapor deposition

A No. 1.5 glass slide, previously plasma-cleaned with a low-pressure plasma system (Diener electronic Plasma-Surface-Technology, ZEPTO), is coated with 1 nm of chromium and 10 nm of gold using a thermal evaporator (the Edwards Coating System E306A) through an H-shaped mask. The horizontal line of the H-mask has a width of 750 $\mu$m (Fig. S1).

### B. Laser ablation

The shark-teeth pattern is made using the setup described in Ref. 48. Although this setup is mainly used for laser ablation experiments,[49] it has also proven useful for laser patterning.[50] Figure S2 shows a simplified schematic overview of the setup. An ultrafast laser system produces laser pulses at a central wavelength of 1034 nm and a pulse duration of 170 ps. A combination of neutral density filters, a polarizing beam splitter, and a half-wave plate controls the pulse energy. For making the shark-teeth electrodes, we set the pulse energy on the sample to ~28 nJ, which is equivalent to a fluence of 0.42 J/cm$^2$. The experiments were conducted using a 100× objective with a numerical aperture (NA) of 0.80 (Nikon CFI60 100×).

After the power control section, the pulses pass two pellicle beam splitters. A microscope objective then focuses the pulses onto the gold surface. The light produced by a green LED is coupled into the beam path using the first of the two pellicle beam splitters. This light illuminates the sample such that the sample can be monitored using the objective, the second pellicle beam splitter, and a CCD camera (Andor iXon3 885). The sample is mounted on a motorized stage.

To make the shark-teeth electrodes, we start with the plain H-sample; see Fig. 1(a). After aligning the sample, we run the laser at an effective repetition frequency of 2 kHz. The start position of the sample is such that the optical axis of the objective is located a short distance (≈50 $\mu$m) from the inner gold strip of the sample and such that the surface of the sample is in the focal plane of the objective. We then open the shutter and start moving the stage at a speed of 10 m/s, such that the full width of the gold strip passes through the focus of the objective. We have chosen this combination of repetition frequency, pulse energy, and stage speed such that the disk-shaped ablation areas slightly overlap [see Figs. 1(b)–1(f)]. When the full gold strip has passed through the focus of the objective, the shutter closes again. As a final step, we visually check the electrode for possible short circuits. Occasionally, incomplete ablation occurs when the two laser beams are spaced farther apart than intended, leaving unablated gold between electrode segments and causing short circuits. These instances are rare and easily identified by inspecting the ablated region using the CCD camera. When detected, we manually ablate the remaining gold by briefly opening the shutter to restore proper electrode separation. This corrective step was required only in a small fraction of samples. We fabricated ~20 samples using this method, all of which successfully underwent particle manipulation and/or ion accumulation experiments without failure.

After the laser ablation step, the samples were used directly in optical microscopy experiments without any additional cleaning.

### C. TIR microscopy

A 640 nm laser beam (Ignis, Laser Quantum) with a power of 60 mW is focused on the back focal plane of an oil-immersion objective (Nikon CFI Apochromat TIRF 60×, 1.49 NA) by a tube lens with a focal length of 200 mm. The focused beam is off-axis so that the beam coming out from the objective could illuminate the sample at a large incidence angle, which enables the total internal reflection to occur at the electrode–electrolyte interface. The total internally reflected light is guided to a position detector (PQD-80A, Thorlabs) to maintain the position of the sample at the focus plane of the objective. The scattered light from the shark-teeth electrode is collected by the same objective and then focused by a tube lens to project it on a scientific CMOS (sCMOS) camera (Hamamatsu ORCA-Flash 4.0 V3).

### D. Fluorescence microscopy

A blue LED (Thorlabs, M395L4) excites the particles, with the excitation light reflected by a dichroic filter toward the microscope objective (ZEISS 40×/0.65). The emitted light travels back through a long-pass dichroic filter (500 nm) to the camera (Hamamatsu Digital Camera, C11440). The camera exposure time is 0.02 s. This setup efficiently filters out the excitation light, allowing clear particle visualization.

### E. Electric field generation

A waveform generator (KEYSIGHT InfiniiVision DSOX2024A) is synchronized with the camera to monitor the applied voltage and circuit, enabling concurrent observation of the particles' response to the applied potential.

### F. Electrolyte solution

Sigma-Aldrich potassium chloride (anhydrous, free-flowing, Redi-Dri™, ACS reagent, ≥99%) is mixed with Ultrapure Type 1 water to prepare a 0.1M electrolyte solution.

### G. Particle solutions

Aqueous suspensions of Fluoresbrite® YG carboxylate microspheres (200 nm in diameter, 2.5% weight/volume), with an excitation peak at 441 nm and an emission peak at 486 nm, are used for particle tracing and trapping experiments via fluorescence microscopy. For trapping experiments using a TIR microscope, Sigma-Aldrich 30 nm gold nanoparticles (OD 1) stabilized in citrate buffer are utilized. Ultrapure (Type 1) water is used to dilute the particles. All solutions are inserted between the electrodes using a clear silicone gasket (3 × 1 mm$^2$) with a well capacity of 3–10 $\mu$l, sourced from Sigma-Aldrich (Grace Bio-Labs reusable CultureWell™ gaskets, product code GBL103250).

### H. SEM

Nanoelectrode morphology is analyzed using a ZEISS EVO 15 SEM operated at 5 kV.

## I. Impedance spectroscopy

Impedance and cyclic voltammetry measurements of the shark-teeth electrodes are conducted using a BioLogic SP300 potentiostat.

## SUPPLEMENTARY MATERIAL

The supplementary material provides additional data on ion accumulation and nanoparticle trapping, videos, microscopy images, control experiments, and details of the experimental setup and electrochemical analysis.

## ACKNOWLEDGMENTS

The authors thank Sjoerd Quaak, Kevin Namink, and Kerman José Gallego Lizarribar for their assistance with some of the earlier measurements for this project. The authors also acknowledge the technical support with the measurement setup from Paul Jurrius, Aron Opheij, Dante Killian, Jan Bonne Aan, Arjan Driessen, and Dave van den Heuvel. This research was supported by Refeyn LTD and Nederlandse Organisatie voor Wetenschappelijk Onderzoek (Grant No. Vici 68047618).

## AUTHOR DECLARATIONS

### Conflict of Interest

The authors have no conflicts to disclose.

### Author Contributions

**Itir Bakis Dogru Yuksel**: Conceptualization (equal); Investigation (equal); Methodology (equal); Visualization (equal); Writing – original draft (equal); Writing – review & editing (equal). **Zhu Zhang**: Data curation (supporting); Investigation (supporting); Methodology (supporting); Software (lead); Visualization (supporting); Writing – review & editing (equal). **Marnix Vreugdenhil**: Investigation (supporting); Methodology (supporting); Writing – original draft (supporting); Writing – review & editing (supporting). **Allard P. Mosk**: Supervision (supporting); Validation (supporting); Writing – review & editing (supporting). **Dries van Oosten**: Conceptualization (supporting); Supervision (supporting); Validation (supporting); Writing – original draft (supporting); Writing – review & editing (supporting). **Sanli Faez**: Conceptualization (equal); Methodology (equal); Supervision (equal); Writing – original draft (equal); Writing – review & editing (equal).

## DATA AVAILABILITY

The data that support the findings of this study are available within the article and its supplementary material.

## REFERENCES

[1] Q. Zhu, Z. Wen, H. Zhan, and S. Yuan, Water Resour. Res. **56**, e2020WR027396, https://doi.org/10.1029/2020wr027396 (2020).
[2] J. Rivnay, S. Inal, B. A. Collins, M. Sessolo, E. Stavrinidou, X. Strakosas, C. Tassone, D. M. Delongchamp, and G. G. Malliaras, Nat. Commun. **7**, 11287 (2016).
[3] P. Sharma, I.-H. Baek, T. Cho, S. Park, and K. B. Lee, Powder Technol. **208**, 7 (2011).
[4] D.-J. Lee, Y.-M. Oh, S.-W. Park, B.-E. Park, and Y.-C. Kim, J. Display Technol. **8**, 361 (2012).
[5] S. Wärmländer, A. Tiiman, A. Abelein, J. Luo, J. Jarvet, K. L. Söderberg, J. Danielsson, and A. Gräslund, ChemBioChem **14**, 1692 (2013).
[6] S. Faez, Y. Lahini, S. Weidlich, R. F. Garmann, K. Wondraczek, M. Zeisberger, M. A. Schmidt, M. Orrit, and V. N. Manoharan, ACS Nano **9**, 12349 (2015).
[7] M. Lipovsek, A. Fierro, E. G. Pérez, J. C. Boffi, N. S. Millar, P. A. Fuchs, E. Katz, and A. B. Elgoyhen, Mol. Biol. Evol. **31**, 3250 (2014).
[8] E. D. B. Foley, M. S. Kushwah, G. Young, and P. Kukura, Nat. Methods **18**, 1247 (2021).
[9] H. Hajjoul, S. Kocanova, I. Lassadi, K. Bystricky, and A. Bancaud, Lab Chip **9**, 3054 (2009).
[10] D. Cole, G. Young, A. Weigel, A. Sebesta, and P. Kukura, ACS Photonics **4**, 211 (2017).
[11] G. Young, N. Hundt, D. Cole, A. Fineberg, J. Andrecka, A. Tyler, A. Olerinyova, A. Ansari, E. G. Marklund, M. P. Collier *et al.*, Science **360**, 423 (2018).
[12] G. Young and P. Kukura, Annu. Rev. Phys. Chem. **70**, 301 (2019).
[13] P. Zhu, P. R. Slater, and E. Kendrick, Mater. Des. **223**, 111208 (2022).
[14] D. J. Arnot, K. S. Mayilvahanan, Z. Hui, K. J. Takeuchi, A. C. Marschilok, D. C. Bock, L. Wang, A. C. West, and E. S. Takeuchi, Acc. Mater. Res. **3**, 472 (2022).
[15] J. D. Yantzi, J. T. W. Yeow, and S. S. Abdallah, Biosens. Bioelectron. **22**, 2539 (2007).
[16] I. B. Dogru-Yuksel, A. P. Mosk, and S. Faez, Nanoscale **16**, 8514 (2024).
[17] K. Sy, N. A. P. Ondevilla, H.-Y. Fang, P.-W. Liu, P.-W. Chen, J.-S. Lin, P.-T. Chen, and H.-C. Chang, Sens. Actuators, B **378**, 133160 (2023).
[18] T. Zhou, J. Chen, E. Kropp, and L. Kulinsky, ACS Appl. Mater. Interfaces **12**, 35647 (2020).
[19] J. Ji, J. Zhang, J. Wang, Q. Huang, X. Jiang, W. Zhang, S. Sang, X. Guo, and S. Li, Biosens. Bioelectron. **165**, 112398 (2020).
[20] V. Varmazyari, H. Habibiyan, H. Ghafoorifard, M. Ebrahimi, and S. Ghafouri-Fard, Sci. Rep. **12**, 12100 (2022).
[21] R. Pan, D. Wang, K. Liu, H.-Y. Chen, and D. Jiang, J. Am. Chem. Soc. **144**, 17558 (2022).
[22] Y. Yang, Y.-X. Ren, M. Chen, Y. Arita, and C. Rosales-Guzmán, Adv. Photonics **3**, 034001 (2021).
[23] C. Yin, X. Jiang, S. Mann, L. Tian, and B. W. Drinkwater, Small **19**, 2207917 (2023).
[24] L. Gong, A. Cretella, and Y. Lin, Biosens. Bioelectron. **236**, 115426 (2023).
[25] K. Namink, X. Meng, M. T. M. Koper, P. Kukura, and S. Faez, Phys. Rev. Appl. **13**, 044065 (2020).
[26] Z. Zhang and S. Faez, Faraday Discuss. **246**, 426 (2023).
[27] J. K. Utterback, A. J. King, L. Belman-Wells, D. M. Larson, L. M. Hamerlynck, A. Z. Weber, and N. S. Ginsberg, ACS Energy Lett. **8**, 1785 (2023).
[28] A. J. Merryweather, C. Schnedermann, Q. Jacquet, C. P. Grey, and A. Rao, Nature **594**, 522 (2021).
[29] B. Chen, H. Zhang, J. Xuan, G. J. Offer, and H. Wang, Adv. Mater. Technol. **5**, 2000555 (2020).
[30] M. Saghafi, S. Chinnathambi, and S. G. Lemay, Curr. Opin. Colloid Interface Sci. **63**, 101654 (2023).
[31] H. Nili and N. Green, *Encyclopedia of Nanotechnology*, 25 (Springer, 2016).
[32] M. Mastrangeli and J. van den Eijnden-van Raaij, Stem Cell Rep. **16**, 2037 (2021).
[33] Y. Li, Y. Wang, K. Wan, M. Wu, L. Guo, X. Liu, and G. Wei, Nanoscale **13**, 4330 (2021).
[34] C. S. Ivanoff, J. J. Wu, H. Mirzajani, C. Cheng, Q. Yuan, S. Kevorkyan, R. Gaydarova, and D. Tomlekova, Biomed. Microdevices **18**, 84 (2016).
[35] J. R. Soucy, A. J. Bindas, A. N. Koppes, and R. A. Koppes, Iscience **21**, 521 (2019).
[36] A. Moya, X. Illa, I. Gimenez, Y. Lazo-Fernandez, R. Villa, A. Errachid, and G. Gabriel, Sens. Actuators, B **255**, 2861 (2018).
[37] P. Tawade and M. Mastrangeli, ChemBioChem **25**, e202300560 (2024).

[38]Y. Lu, T. Liu, A. C. Lamanda, M. L. Y. Sin, V. Gau, J. C. Liao, and P. K. Wong, SLAS Technol. **20**, 611 (2015).
[39]Z. Zhang, J. Yang, C. Lian, and S. Faez, J. Phys. D: Appl. Phys. **54**, 384005 (2021).
[40]A. Peters, Z. Zhang, and S. Faez, HardwareX **14**, e00424 (2023).
[41]E. Abram, I. Milov, N. Orlov, K. Van Druten, E. C. Garnett, and P. Planken, Opt. Express **32**, 4564 (2024).
[42]G. Givirovskiy, V. Ruuskanen, L. S. Ojala, M. Lienemann, P. Kokkonen, and J. Ahola, Heliyon **5**, e01690 (2019).
[43]C. Wen, S. Schmid, and C. Dekker, ACS Nano **18**, 20449 (2024).
[44]I. I. Hosseini, M. Moghimi Zand, A. A. Ebadi, and M. Fathipour, Sci. Rep. **11**, 2341 (2021).
[45]R. Grange, F. Dutto, and A. Radenovic, *Niobates Nanowires: Synthesis, Characterization and Applications* (InTech, 2011).
[46]H. Zhang, H. Chang, and P. Neuzil, Micromachines **10**, 423 (2019).
[47]P. V. Tawade, H. Aydogmus, L. Ivancevic, J.-J. Yeh, V. Gkouzioti, J.-P. Frimat, J. Den Toonder, and M. Mastrangeli, in *2025 IEEE 38th International Conference on Micro Electro Mechanical Systems (MEMS)* (IEEE, 2025), pp. 426–429.
[48]M. Vreugdenhil and D. van Oosten, Rev. Sci. Instrum. **93**, 073003 (2022).
[49]M. Vreugdenhil and D. Van Oosten, *Laser-Induced Damage in Optical Materials*, 12726 (SPIE, 2023), p. 66.
[50]L. Cruciani, M. Vreugdenhil, S. van Vliet, E. Abram, D. van Oosten, R. Bliem, K. van Druten, and P. Planken, Appl. Phys. Lett. **124**, 171902 (2024).